Energy & Environmental Science

ROYAL SOCIETY OF CHEMISTRY

PAPER

View Article Online
View Journal | View Issue

Cite this: *Energy Environ. Sci.*, 2026, **19**, 2333

Synergistic steric–dipole modulation *via* stepwise trifluoromethyl substitution enables active-layer hierarchical assembly and >20% power conversion efficiency in organic photovoltaic devices

Jie Wang,†[a] Xin Chen,†[a] Jingyi Huo,[a] Jiong Yang,[a] Longyu Li,[a] Wendi Shi,[a] Ruibin Bian,[a] Wenkai Zhao,[b] Guankui Long,[b] Zhaoyang Yao,[a] Chenxi Li,[a] Xiangjian Wan *[a] and Yongsheng Chen *[a]

Received 2nd December 2025,
Accepted 9th March 2026

DOI: 10.1039/d5ee07321a

rsc.li/ees

Rational molecular design can effectively optimize the fineness of phase separation and vertical phase gradients of organic solar cells (OSCs), thereby boosting exciton dissociation kinetics and device efficiency. The "$C^{\delta+}$–$F^{\delta-}$" polarity of $-CF_3$ promotes diverse noncovalent interactions, providing a key driving force for ordered assembly of active layer morphology. Herein, three acceptors (named CHE-*n*F *n* = 3, 6, 9) were synthesized by stepwise $-CF_3$ functionalization of CHE-Me, progressively enhancing steric and molecular dipole effects, while continuously reducing surface energy. Research indicates that increased steric hindrance suppresses acceptor over-aggregation, thereby optimizing domain size. Enhanced dipoles strengthen donor/acceptor (D/A) interactions, shorten π–π stacking distances, accelerate exciton dissociation, and mitigate trap-assisted recombination; while minimized surface energy induces vertical phase gradients that facilitate charge transport. The steric–dipole–surface energy synergistic regulation strategy yielded an optimized morphology, delivering a power conversion efficiency (PCE) of 19.32% (fill factor (FF) of 82.06%) for the CHE-9F device, 20.30% for the ternary device, and 16.69% for the module. This work establishes a molecular steric–dipole regulation strategy for the precise control of phase separation and vertical composition gradients in photoactive layers, providing an effective pathway for high-performance OSCs.

Broader context

The bottleneck of improvement of organic solar cell (OSC) power conversion efficiencies (PCEs) lies in the difficulty of precisely regulating the microscale arrangement of materials within the active layer, which directly impacts charge transport efficiency and energy output. Different from previous studies focusing on single-site functional modification, this work innovatively adopts a stepwise trifluoromethylation strategy. By tuning molecular steric hindrance, polarity, and surface energy, this strategy effectively suppresses excessive material aggregation, optimizes the uniformity of microscale arrangement, and enhances charge transport capability. Notable achievements are achieved: the binary device exhibits a PCE of 19.32%, the ternary device's PCE is further improved to a maximum of 20.30%, and the 13.5 cm^{-2} scalable module delivers a PCE of 16.69%.

Introduction

The power conversion efficiency (PCE) of organic solar cells (OSCs) has steadily advanced, largely driven by molecularly engineered active-layer materials, particularly small-molecule acceptors (SMAs) and device optimization.[1–7] While optimizing intramolecular photoelectric properties is essential, the nanoscale donor/acceptor (D/A) phase separation in the active layer predominantly governs charge transfer dynamics, thereby determining exciton dissociation, charge extraction, and recombination.[8,9] For efficient exciton diffusion and dissociation, the characteristic phase-separation length must not exceed the exciton diffusion length, highlighting the importance of both domain size and interfacial area.[10] In addition, vertical phase separation critically affects device performance, where an ideal gradient, with donor-rich regions near the anode and acceptor-rich regions adjacent to the cathode,

[a] *State Key Laboratory of Elemento-Organic Chemistry, Frontiers Science Center for New Organic Matter, The Centre of Nanoscale Science and Technology and Key Laboratory of Functional Polymer Materials, Institute of Polymer Chemistry, Renewable Energy Conversion and Storage Center (RECAST), Tianjin Key Laboratory of Functional Polymer Materials, Nankai University, Tianjin, 300071, China. E-mail: xjwan@nankai.edu.cn, yschen99@nankai.edu.cn*

[b] *School of Materials Science and Engineering, National Institute for Advanced Materials, Nankai University, Tianjin, 300071, China*

† These authors contributed equally.

facilitates directional charge transport and reduces interfacial recombination.[11,12] Despite extensive efforts devoted to precisely manipulating the BHJ morphology through innovative material design and advanced processing strategies to enhance the PCE,[13–17] achieving simultaneous control over multiscale phase structures and vertical composition gradients within the active layer remains a formidable challenge toward highly efficient OSCs.[18]

Accordingly, rational molecular design of SMAs represents a central avenue for concurrently modulating electronic structures and directing morphological evolution toward well-defined phase separation and vertical stratification. Guided by this concept, incorporation of functional motifs such as $-CF_3$ offers an effective means to synergistically optimize optoelectronic properties and nanoscale morphology.[19–23] The $-CF_3$, with its characteristic "$C^{\delta+}$–$F^{\delta-}$" polarization,[24,25] enables diverse noncovalent interactions with donor polymers such as PM6 through several mechanisms (Fig. 1a): (1) the strongly electron-withdrawing fluorine atoms generate electrostatic complementarity with electron-rich regions of PM6; (2) the high polarizability of the C–F bond facilitates dipole–induced dispersion interactions with the PM6 backbone, especially in low-dielectric organic films; and (3) the trigonal pyramidal geometry of $-CF_3$ permits multi-point contacts (such as F···F

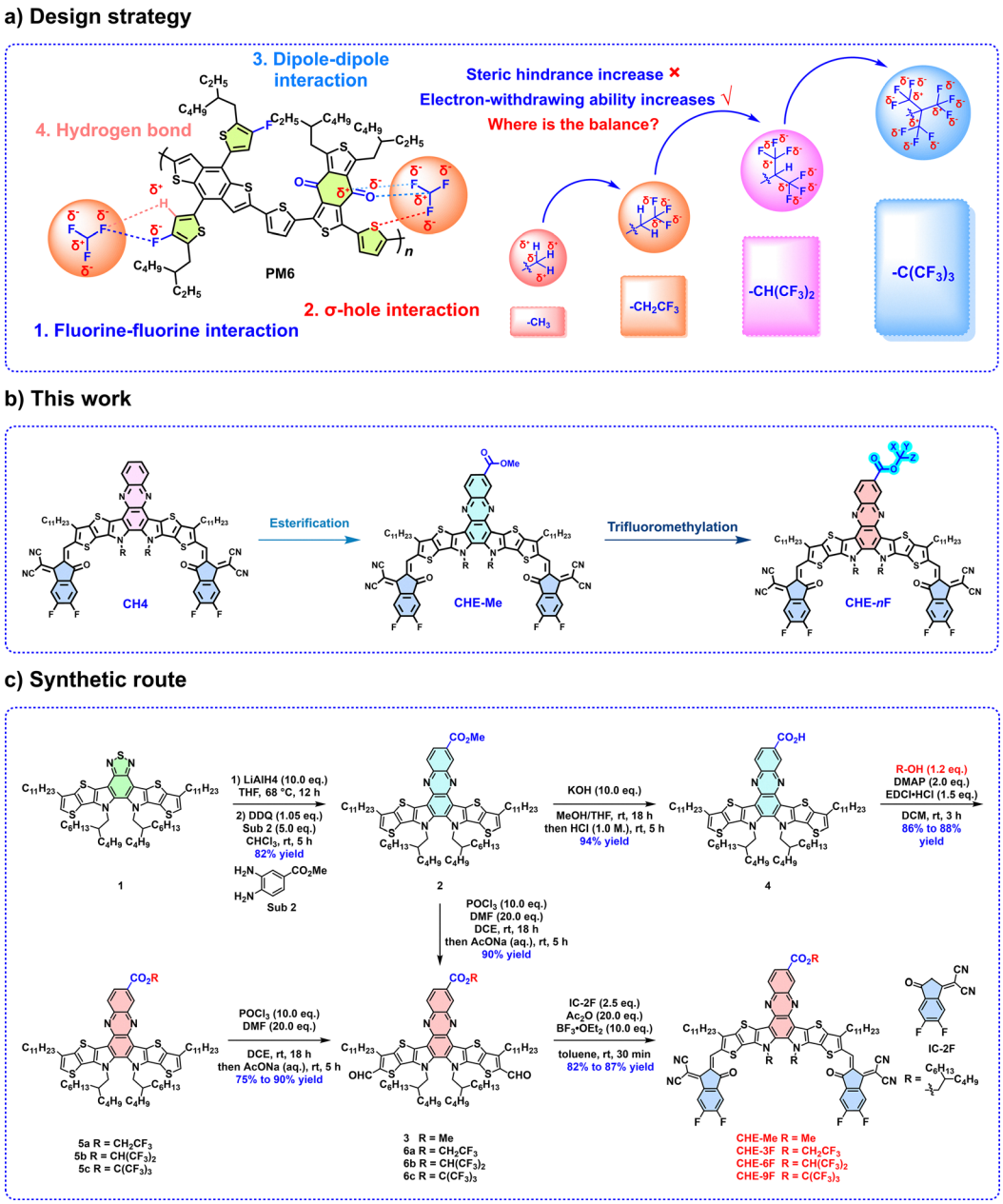

Fig. 1 (a) Multiple potential noncovalent interactions between $-CF_3$ and PM6. (b) Chemical structures of CH_4, CHE-Me and CHE-*n*Fs. (c) Corresponding synthetic routes for the four SMAs.

and F···O interactions), thereby enhancing cooperative intermolecular interactions. Guided by these considerations, we hypothesized that the strategic incorporation of $-CF_3$ units into SMAs could effectively strengthen the D/A interactions, thereby simultaneously optimizing the probe optoelectronic properties and active-layer morphology.

Thus, in this work, we designed and synthesized three $-CF_3$ functionalized SMAs (CHE-*n*F, *n* = 3, 6, 9; Fig. 1b) *via* a stepwise trifluoromethylation strategy to systematically investigate the impact of $-CF_3$ incorporation on the molecular structure, aggregation behavior, and active-layer morphology. Progressive substitution from $-CF_3$ to $-C(CF_3)_3$ was found to enhance steric hindrance and dipole moment while reducing surface energy. These effects act synergistically through three key mechanisms: (1) steric hindrance suppresses excessive aggregation, optimizes domain size and uniformity, and minimizes trap formation; (2) enhanced dipoles strengthen D/A interactions, shorten π–π stacking distances, accelerate exciton dissociation, and mitigate trap-assisted recombination; and (3) reduced surface energy drives vertical phase gradients that promote directional charge transport and improve charge collection. As a result, PM6/CHE-nF devices exhibit notable improvements in efficiency, with CHE-9F delivering a champion PCE of 19.32% (V_{oc} = 0.898 V, J_{sc} = 26.22 mA cm^{-2}, FF = 82.06%). Furthermore, the ternary PM6:Bo-4Cl:CHE-9F blend achieves an enhanced PCE of 20.01%, while the corresponding 13.5 cm^2 module delivers a PCE of 16.69%. To further assess the general applicability of this approach, To further assess the general applicability of this approach, 20 mol% CHE-9F was incorporated into the PM6:Bo-4Cl and PM6:btp-eC9 blend system, and 10 mol% CHE-9F into the D18:L8-BO blend system, further enhances the PCE to 20.10% and 20.30%. These findings demonstrate that stepwise trifluoromethyl substitution provides an effective steric–dipole regulation strategy to precisely tailor molecular packing, phase separation, and vertical stratification, thereby markedly advancing the performance of OSCs.

Result and discussion

The synthetic routes of the four SMAs are illustrated in Fig. 1c, with detailed optimization procedures provided in the SI. Initially, commercially available compound 1 was reduced with $LiAlH_4$, followed by oxidation with DDQ and *in situ* condensation with methyl 3,4-diaminobenzoate, affording the esterified quinoxaline central unit intermediate 2 in an overall yield of 82%.[26] Subsequent hydrolysis converted 2 into the carboxylated central unit intermediate 4 with a yield of 94%. Intermediate 4 was then subjected to modified Steglich esterification with various fluorinated alcohols to produce the corresponding trifluoromethylated intermediates 5a–5c in 86–88% yields. Thereafter, Vilsmeier–Haack formylation afforded the dialdehyde intermediates (3–6c) in 75–90% yields, which were finally subjected to Knoevenagel condensation with IC-2F to yield the target SMAs in 82–87% yields. This divergent synthetic strategy enables precise control over the number and position of $-CF_3$ in the central unit, allowing efficient construction of trifluoromethylated SMAs. The structures and purities of all new compounds were confirmed by $^1H/^{13}C/^{19}F$ NMR spectroscopy and MALDI-TOF mass spectrometry.

To investigate the effect of stepwise trifluoromethylation on molecular structures and frontier orbitals, DFT calculations were performed to optimize the geometries of four SMAs and analyze their electrostatic potential (ESP) distributions. As shown in Fig. S1, all molecules feature small N–C–C–N dihedral angles ($\sim 9^\circ$), which gradually increase from CHE-Me to CHE-9F owing to the increasing steric hindrance. Simultaneously, as substituents change from weak electron donors to strong electron-withdrawing groups, the dipole moments of the central units increase (Fig. 2a and Fig. S2). Notably, in the CHE-*n*F series, the dipole vectors pointed from the molecular center toward end groups, in contrast to CHE-Me. This is attributed to the strong electron-withdrawing inductive effect of $-CF_3$, which modulates backbone electron distribution *via* the carbonyl, reduces the central unit's electron-donating ability, and enhances sensitivity to end-group modification. The increased dipole moments are expected to facilitate exciton dissociation, suppress charge recombination, and promote directional charge transport.[27] As shown in Fig. 2b, all four SMAs with frontier orbital charges exhibiting a ''peak–valley–peak'' pattern.[28] Compared with CHE-Me, increasing trifluoromethyl substituents shifts the positions of electron-donating and -withdrawing centers along the backbone. Specifically, asymmetric $-CH(CF_3)_2$ induce pronounced charge fluctuations in CHE-6F, whereas symmetric $-CF_3$ lead to discrete charge localization, and bulky $-C(CF_3)_3$ cause only minor perturbations, resulting in limited effects on molecular orbitals.

Thermal analysis further revealed the impact of stepwise trifluoromethylation. TGA curves (Fig. S3) show that four SMAs exhibit excellent thermal stability, with decomposition temperatures (T_d, 5% weight loss) exceeding 320 °C, specifically 342 °C, 334 °C, 334 °C, and 323 °C, respectively. DSC measurements indicate that the melting temperatures (T_m) of CHE-*n*F acceptors are lower than that of CHE-Me (>300 °C) and decrease systematically with increasing *n*, from 292.6 °C to 278.0 °C (Fig. 2c). This indicates that increasing the number of $-CF_3$ restricts intermolecular packing due to steric hindrance, weakens intermolecular interactions, and consequently lowers the T_m.[29]

As shown in Fig. 2d and Fig. S4, the molar extinction coefficients (ε) gradually increase from CHE-Me to CHE-9F (2.08×10^5 to 2.30×10^5 M^{-1} cm^{-1}) in chloroform solution, indicating that the enhanced electron-withdrawing ability significantly strengthens the intramolecular charge transfer (ICT) effect. Temperature-dependent absorption measurements (Fig. S5) demonstrate that increasing the steric bulk of substituents results in a more pronounced thermally induced disaggregation effect (with a larger blue-shift magnitude), which confirms that the bulky $-C(CF_3)_3$ can effectively modulate intermolecular interactions. In films (Fig. 2e), the absorption peaks exhibit a redshift, while the wavelength shift ($\Delta\lambda$) between the film and solution gradually decreases with increasing $-CF_3$ content (75 to 62 nm), suggesting that steric hindrance

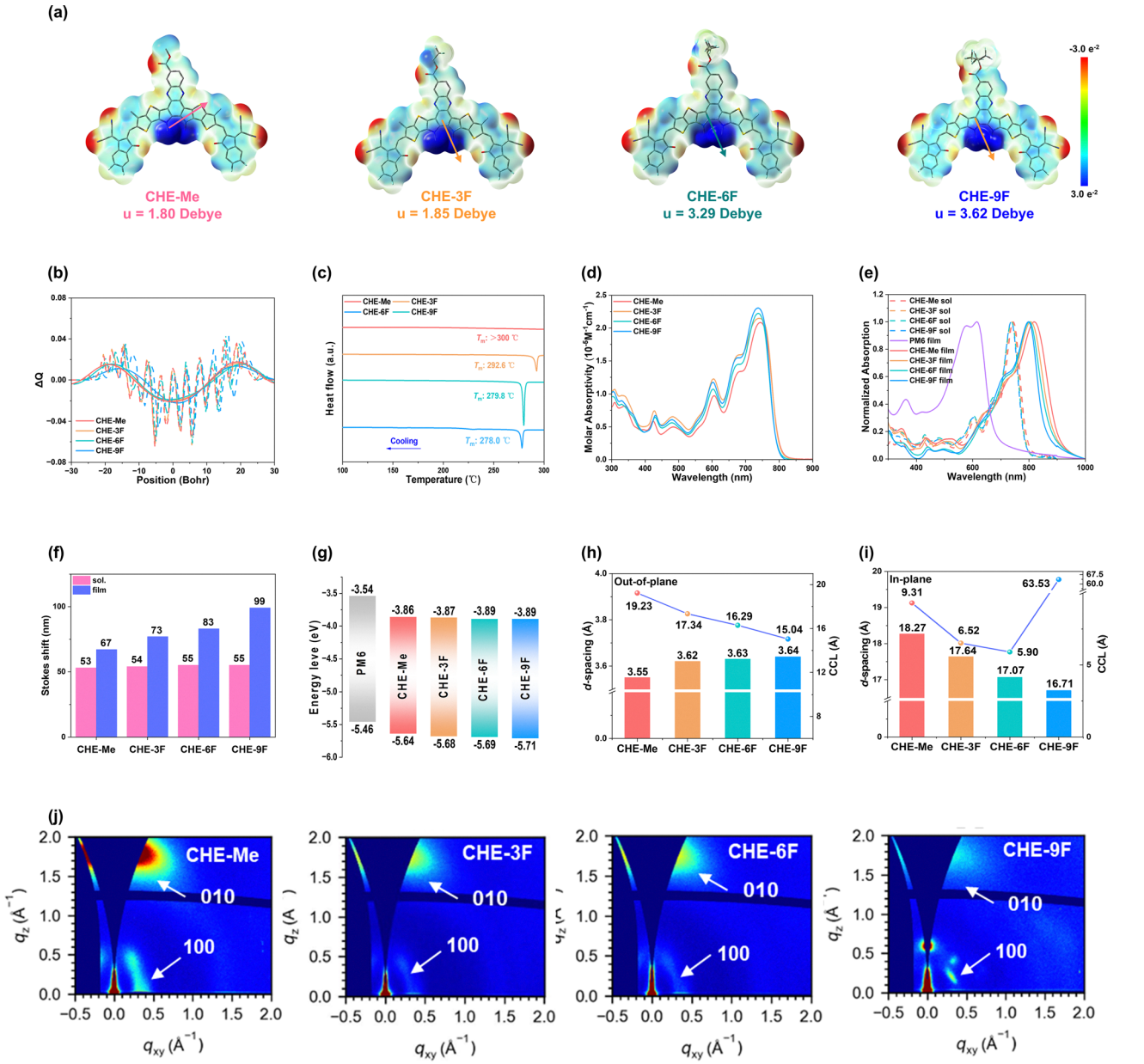

Fig. 2 (a) DFT-calculated ESP distribution and dipole moment of four SMAs. (b) Theoretically calculated frontier orbital charge density differences (Δ*Q*). (c) DSC curves of four SMAs at a heating rate of 10 K min^{-1}. (d) Absorption spectra of four SMAs in chloroform solution. (e) Normalized absorption spectra of four SMAs in solutions and neat films. (f) Bar charts of Stokes shifts for four SMAs in solution and neat films. (g) Energy level diagram of four SMAs. (h) and (i) Statistical analysis of *d*-spacing and CCL for neat films of four SMAs in the OOP and IP directions. (j) 2D GIWAXS patterns of four SMAs at neat films.

suppresses disordered intermolecular aggregation and weakens intermolecular interactions, consistent with the observed decrease in T_m. Stokes shift analysis (Fig. 2f and Fig. S6) shows that, in solution, the solvation shell effectively screens the electrostatic potential of the substituents, rendering polarity changes minimally influential on excited-state relaxation (fluctuation within ±1 nm). In contrast, in films, increasing –CF_3 content enhances the molecular dipole moment, facilitating the formation of intermolecular charge transfer (CT) states,[30] lowering the excited-state energy, and inducing a redshift in the emission spectrum. Simultaneously, the steric hindrance of the substituents locks the molecular conformation, promotes more ordered aggregated structures, and enhances excited-state charge separation, further amplifying the emission redshift.[31,32]

As shown in Fig. 2g, Fig. S7 and Table S2, cyclic voltammetry (CV) measurements of the PM6 donor and the stepwise trifluoromethylated SMAs reveal that the gradual introduction of –CF_3 slightly lowers both the HOMO and LUMO energy levels (CHE-Me: −3.86/−5.64 eV; CHE-3F: −3.87/−5.68 eV; CHE-6F: −3.89/−5.69 eV; CHE-9F: −3.89/−5.71 eV). This observation agrees well with the DFT calculation results shown in Fig. S8, indicating that –CF_3 substitution enhances the electron-accepting

ability of the molecules and slightly increases the HOMO/LUMO energy gap.

To further investigate the aggregation behavior of the four SMAs, grazing incidence wide-angle X-ray scattering (GIWAXS) measurements were conducted on their neat films (Fig. 2g and Table S3). The results show that four SMAs films adopt a typical face-on orientation, with distinct out-of-plane (OOP) and in-plane (IP) diffraction peaks, indicating that the conjugated backbones preferentially stack perpendicular to the substrate.[33] With stepwise trifluoromethylation, the OOP π–π stacking distances slightly increase (3.55 to 3.64 Å), and the crystalline coherence lengths gradually decrease (19.23 to 15.04 Å), suggesting that steric hindrance limits tight vertical packing. In contrast, the IP π–π stacking distances decrease with increasing $-CF_3$ content (18.27 to 16.71 Å), and CHE-9F exhibits a significantly extended IP crystalline coherence length (63.53 Å), indicating that enhanced molecular dipoles and multiple noncovalent interactions promote long-range IP ordering. Stepwise trifluoromethylation suppresses excessive vertical π–π stacking while enhancing IP ordering through dipole-driven interactions, leading to a morphology that may favor exciton dissociation and directional charge transport,[34] potentially benefiting the performance of OSCs.

To gain atomic-level insight into the effects of stepwise trifluoromethylation on the intrinsic structure and aggregation of SMAs, diffraction-quality single crystals of CHE-Me, CHE-3F, and CHE-6F were obtained, and their crystallographic parameters were analyzed (Table S4). The structures reveal that increasing $-CF_3$ substitution enhances molecular dipoles, which not only modulate the electron density around the ester groups but also directionally redistribute electron density along the carbonyls from the backbone to the end groups. As shown in Fig. 3a, this dipole modulation shortens the carbonyl-α hydrogen distances from 2.620 Å in CHE-Me to 2.366 Å in CHE-3F and further to 1.934 Å in CHE-6F, directly influencing intramolecular electronic interactions. Concurrently, the increased steric hindrance amplifies spatial repulsion between the carbonyl groups and the backbone, leading to stepwise increases in dihedral angles (CHE-Me: 12.54°, CHE-3F: 12.67°, CHE-6F: 15.29°). Notably, the introduction of the bulky $-CH(CF_3)_2$ induces carbonyl configuration inversion, further altering molecular conformation and potentially affecting charge transport and carrier dynamics.

Single-crystal analysis further reveals how stepwise trifluoromethylation regulates molecular packing. CHE-Me and CHE-3F, with similar carbonyl conformations, adopt comparable three-dimensional network packing, with CHE-Me exhibiting rectangular packing voids of approximately 11.715 × 22.272 Å and CHE-3F of 12.986 × 23.106 Å. With increasing steric hindrance, CHE-6F displays a looser two-dimensional packing feature (Fig. 3b). The three SMAs exhibit "end-to-end (E/E)," "end-to-center (E/C)," and "end-to-backbone (E/B)" three primary packing modes,[35] as summarized in Fig. 3c. In the E/B mode, the $-CF_3$, *via* dipole interactions, shorten interlayer distances, decreasing the packing distance from 3.378 Å in CHE-Me to 3.080 Å in CHE-6F. In contrast, in the E/C mode, steric effects dominate, and the bulky $-CH(CF_3)_2$ in CHE-6F significantly increases the packing distance to 3.978 Å, compared with 3.773 Å in CHE-Me and 3.816 Å in CHE-3F. In the E/E mode, where $-CF_3$ does not participate in direct interactions, the packing distances of all three SMAs are similar (CHE-Me: 3.370 Å, CHE-3F: 3.366 Å and CHE-6F: 3.373 Å).

Notably, in the packing of CHE-3F, a three-dimensional "covalent lock" structure, mediated by interlayer and intralayer noncovalent interactions induced by $-CF_3$, is observed for the first time. In contrast, CHE-Me lacks peripheral electrostatic-functional groups, and the bulky $-CH(CF_3)_2$ in CHE-6F hinders the formation of this structure due to pronounced steric effects, so neither exhibits this 3D packing (Fig. 3d). Crystal analysis indicates that stepwise trifluoromethylation can simultaneously modulate the intrinsic molecular conformations and packing modes, where enhanced dipole effects and steric hindrance cooperatively regulate intramolecular electronic interactions and intermolecular aggregation, thereby determining the solid-state organization of the acceptor molecules. This strategy enables precise control over SMAs packing and is of critical significance for improving the performance of organic photovoltaic devices.

OSCs were fabricated using the conventional architecture ITO/2PACz/PM6:SMAs/PNDIT-F3N/Ag. Representative current density–voltage (*J–V*) curves and external quantum efficiency (EQE) spectra are shown in Fig. 4a and b, with the corresponding photovoltaic parameters summarized in Table 1. Compared to the control device based on CHE-Me (PCE = 18.64%), all CHE-*n*F-based devices exhibited enhanced performance, with maximum PCE of 19.08%, 19.25%, and 19.32% for CHE-3F, CHE-6F, and CHE-9F, respectively. As the number of $-CF_3$ substituents increased, the V_{oc} gradually rose and then plateaued (0.885 to 0.899 V). EQE spectra indicate an enhanced photoresponse across 360 to 820 nm, accompanied by a slight blue-shift in absorption, which increases the J_{sc} from 26.28 mA cm^{-2} for CHE-Me to 26.86 mA cm^{-2} for CHE-3F, followed by a modest decrease to 26.22 mA cm^{-2} for CHE-9F. Meanwhile, the FF steadily improved with $-CF_3$ substitution, reaching 82.09% for CHE-9F, while CHE-3F and CHE-6F showed moderate increases of 79.65% and 79.90%, respectively. These trends suggest that stepwise trifluoromethylation strengthens molecular dipole interactions and fine-tunes blend morphology, thereby facilitating exciton dissociation and charge transport. The effect is most pronounced for the bulky $-C(CF_3)_3$ substituent, which synergistically optimizes V_{oc}, J_{sc}, and FF, resulting in the highest overall photovoltaic performance for CHE-9F-based devices (Fig. 4c).

We systematically evaluated the energy loss (E_{loss}) of the devices (see Table S6) based on the Shockley–Queisser (SQ) theory.[36–38] Interestingly, although the optical bandgap (E_g) gradually increases from CHE-Me to CHE-9F, E_{loss} remains nearly constant at ~0.53 eV (Fig. 4d and Fig. S9). This behavior can be attributed to the synergistic regulation of molecular dipole and steric effects induced by stepwise trifluoromethylation. As shown in Fig. 4e and f, ΔE_1 remains essentially unchanged at ~0.265 eV, whereas ΔE_2 and ΔE_3 display opposing trends: ΔE_2 decreases from 0.063 eV for CHE-Me to 0.027 eV for CHE-3F, then increases to 0.036 eV and 0.041 eV for CHE-6F

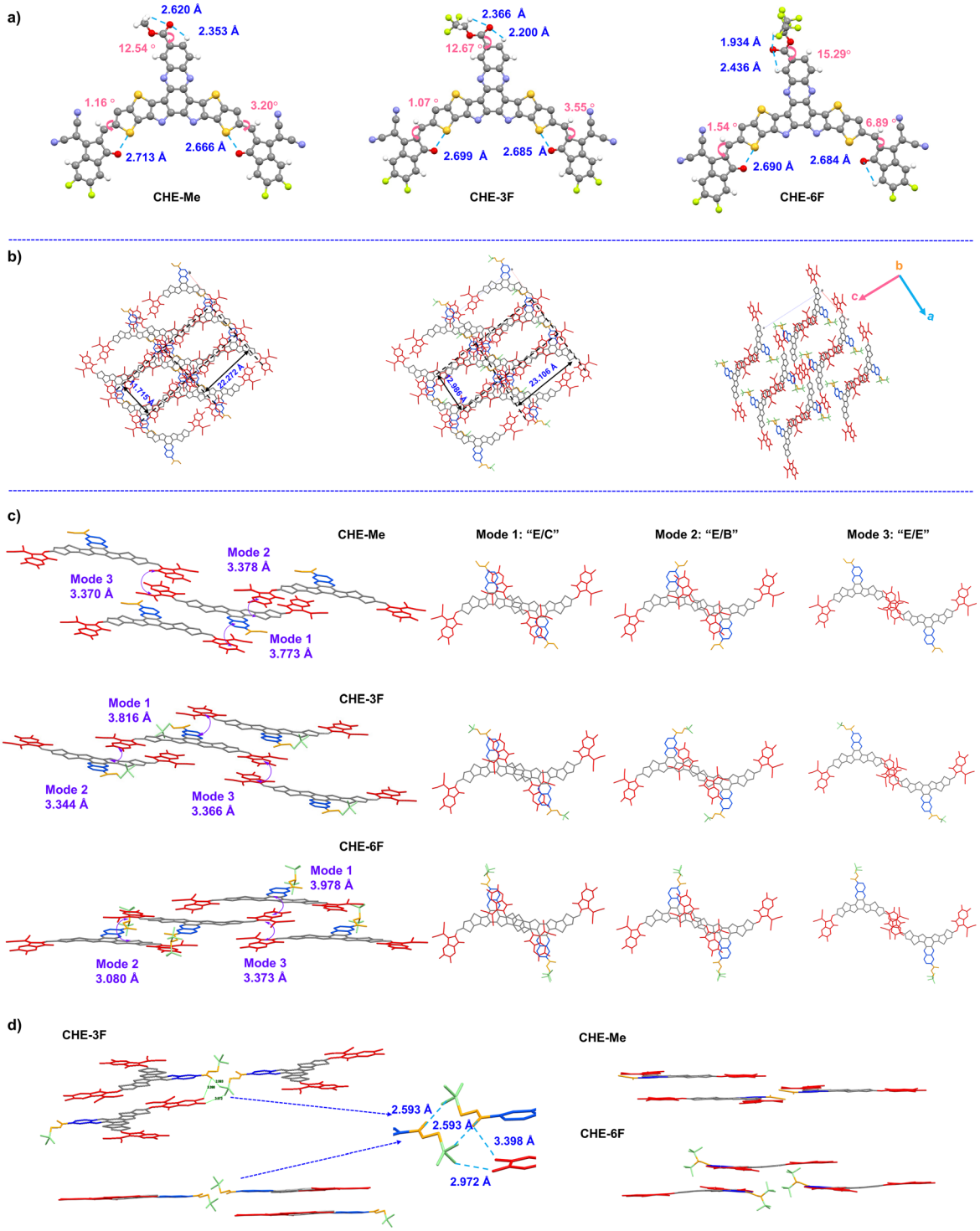

Fig. 3 (a) Molecular structures of the three SMAs. (b) Crystal packing topological structures from top view. (c) The main intermolecular packing modes with intermolecular potential over 70 kJ mol^{-1}. Note that the alkyl substitutions on SMAs were omitted for a clearer presentation. (d) Novel three-dimensional intermolecular interactions exhibited by CHE-3F.

and CHE-9F, respectively; ΔE_3 slightly rises from 0.198 eV for CHE-Me to 0.236 eV for CHE-3F, followed by a decrease to 0.224 eV and 0.221 eV for CHE-6F and CHE-9F, this is consistent with the variation trend of the photoluminescence quantum yield (PLQY, Fig. S10).[39] These observations suggest that moderate $-CF_3$ substitution enhances molecular dipoles, optimizing interfacial CT state energetics and thereby reducing radiative recombination losses (ΔE_2),[40] whereas bulkier substituents primarily introduce steric effects that modulate molecular packing and phase separation, effectively suppressing

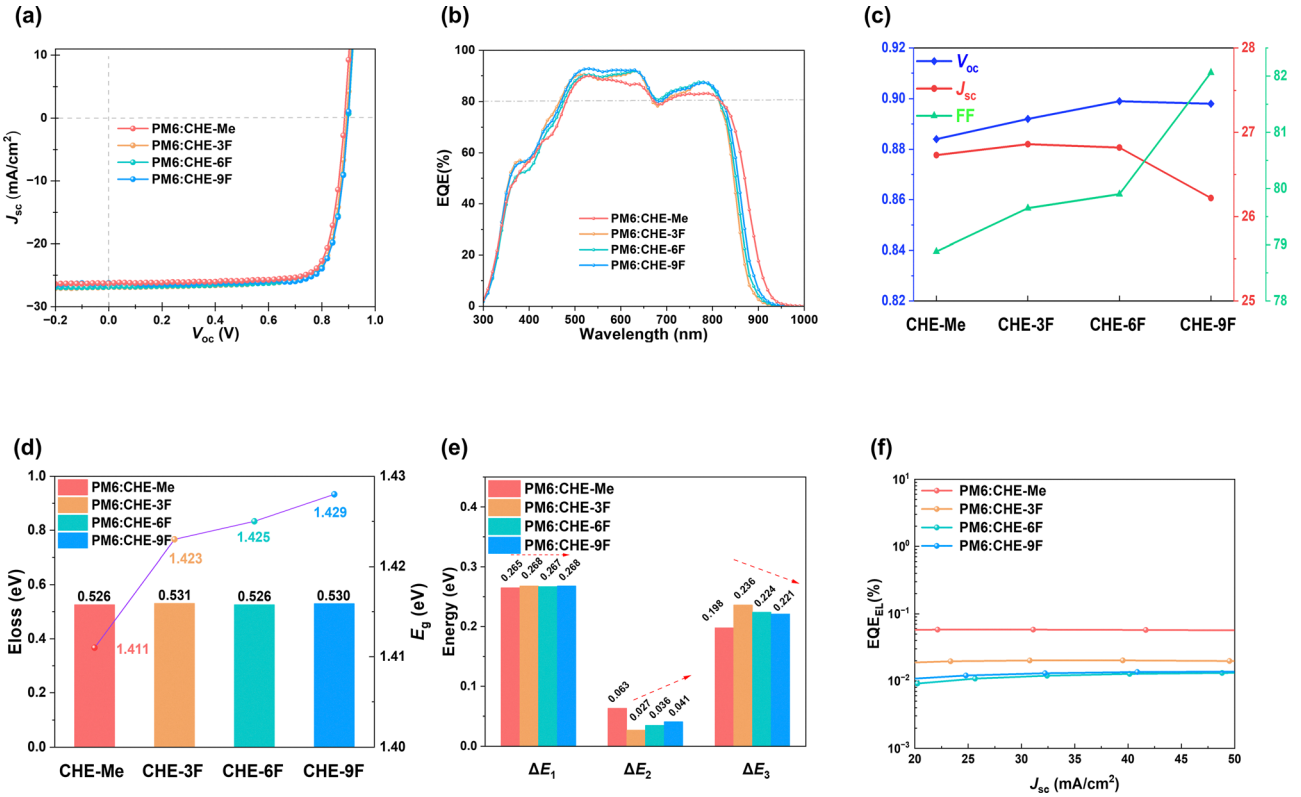

Fig. 4 (a) J–V characteristics of PM6:SMAs OSCs. (b) Corresponding EQE spectra. (c) Comparison of the photovoltaic parameters of four SMAs based OSCs. (d) Summary of photovoltaic band gap (E_g) and energy loss (E_{loss}) diagrams for four SMAs-based OSCs. (e) E_{loss} analysis diagram spectra for the optimized devices. (f) EQE$_{EL}$ *versus* J_{sc} curve.

Table 1 Summary of the device parameters for optimized OSCs[a]

Entry	V_{oc} (V)	J_{sc} (mA cm^{-2})	$J_{sc}^{cal.}$ (mA cm^{-2})	FF (%)	PCE (%)
PM6:CHE-Me	0.884 (0.885 ± 0.002)	26.73 (26.68 ± 0.26)	26.04	78.88 (78.53 ± 1.00)	18.64 (18.55 ± 0.11)
PM6:CHE-3F	0.892 (0.896 ± 0.003)	26.86 (26.49 ± 0.35)	26.25	79.65 (79.29 ± 0.83)	19.08 (18.81 ± 0.16)
PM6:CHE-6F	0.899 (0.893 ± 0.006)	26.82 (28.37 ± 0.35)	25.64	79.90 (80.05 ± 0.54)	19.25 (18.84 ± 0.17)
PM6:CHE-9F	0.898 (0.899 ± 0.004)	26.22 (26.12 ± 0.35)	25.44	82.06 (80.90 ± 0.75)	19.32 (18.99 ± 0.17)

[a] Average parameters calculated from 8 independent OSCs.

trap-assisted recombination and lowering nonradiative losses (ΔE_3).[41–43] Taken together, the complementary action of dipole and steric effects stabilizes E_{loss} across the series, providing mechanistic insights for the rational design of high-performance organic photovoltaic materials.

Furthermore, the initial operational stability of the fabricated OSCs was evaluated under the maximum power point (MPP) condition (Fig. S11). After continuous testing for 200 h under the MPP condition, the PCE of the CHE-Me-based device decayed drastically, retaining only 58% of its initial value. In contrast, the CHE-*n*F-based devices exhibited much better operational stability, with their PCEs remaining at 76% of the initial values. These results indicate that the electrostatic interactions induced by the trifluoromethyl functionalization of the acceptor core unit also play a crucial role in enhancing the operational stability of OSCs.

The hole (μ_h) and electron (μ_e) mobilities of the blend films were measured using the space-charge-limited current (SCLC) method (Fig. 5a and Fig. S12). Compared to the control device based on CHE-Me (μ_h/μ_e = 8.80 × 10^{-4}/2.99 × 10^{-4} cm^2 V^{-1} s^{-1}), all CHE-*n*F-based devices exhibited a progressive increase in μ_e with increasing –CF$_3$ content, reaching 5.16 × 10^{-4}, 7.30 × 10^{-4}, and 8.47 × 10^{-4} cm^2 V^{-1} s^{-1} for CHE-3F, CHE-6F, and CHE-9F, respectively, while μ_h remained nearly constant (8.38 to 8.76 × 10^{-4} cm^2 V^{-1} s^{-1}). As a result, the charge balance factor (μ_h/μ_e) improved significantly from 2.94 for CHE-Me to 1.01 for CHE-9F. This enhancement can be attributed to the dual effects of stepwise trifluoromethylation: (1) the increased electron-withdrawing ability lowers the LUMO energy level, facilitating electron injection, and (2) multiple noncovalent interactions promote improved molecular ordering within the blend films, as reflected by the increased OOP coherence length.

Photocurrent density (J) *versus* effective voltage (V_{eff}) measurements were performed to evaluate exciton dissociation (P_{diss}) and charge collection efficiencies (P_{coll}) (Fig. 5b).[44] Compared to CHE-Me (P_{diss}/P_{coll} = 93.86%/84.86%), CHE-*n*F-based

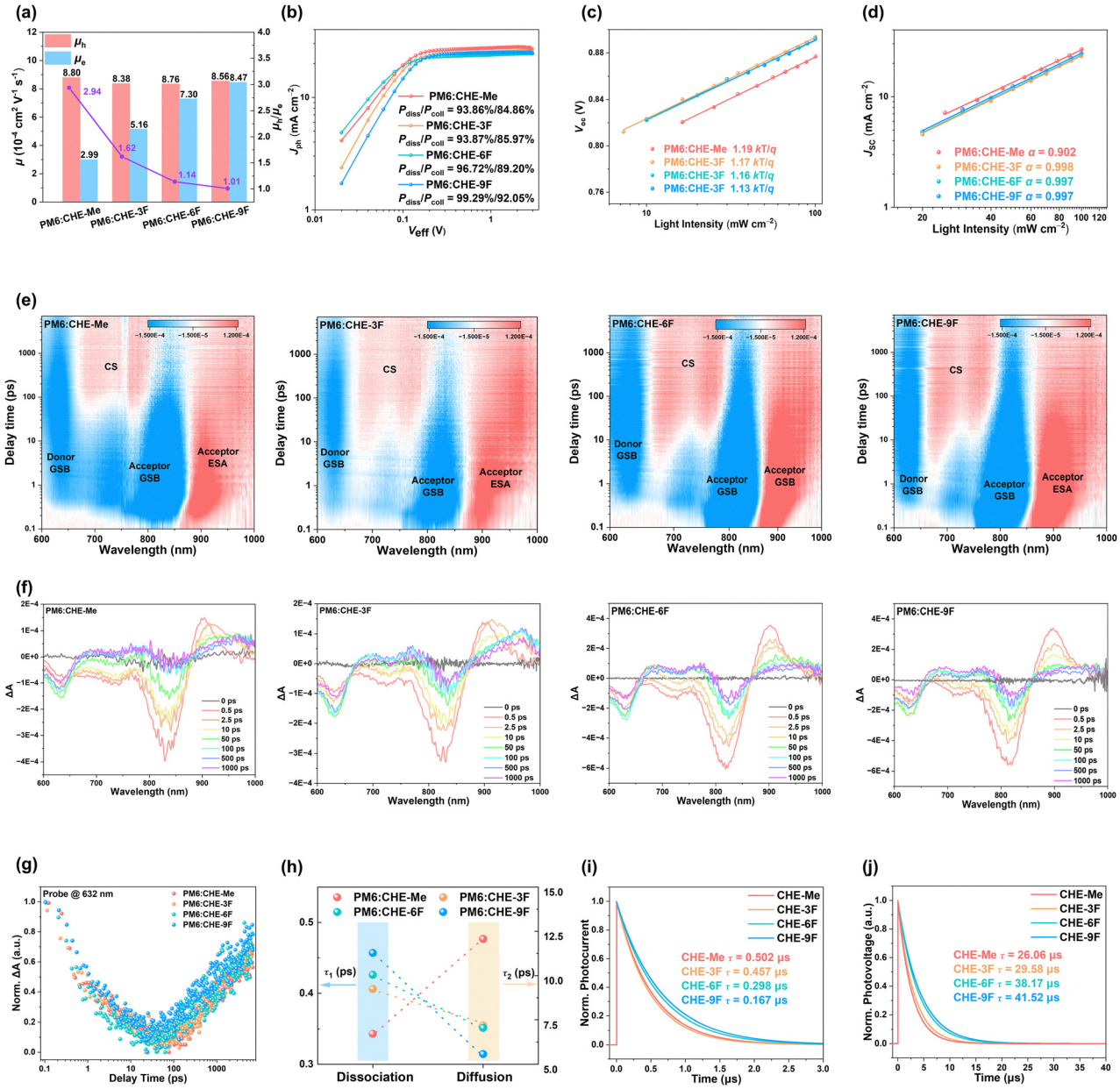

Fig. 5 (a) Electron and hole mobilities of four SMAs of blend films derived from the space-charge-limited current (SCLC) measurements. (b) J_{ph} *versus* V_{eff} curves indicating P_{diss} and P_{coll}. (c) P_{light} dependence of V_{oc}. (d) P_{light} dependence of J_{sc}. (e) Color plots the fs-TA spectra of the PM6/acceptors blend films. (f) Corresponding TA spectra from panels. (g) TA kinetics of the PM6/acceptors blend films. (h) Exciton dynamics time achieved through a biexponential fitting for different blend films. (i) and (j) TPC/TPC decay curves.

devices exhibited progressively enhanced values of 93.87%/85.97%, 96.72%/89.20%, and 99.29%/92.05%, consistent with the increase in fluorescence quenching efficiencies (η_{PLQ}) from 94.7% to 98.3% (Fig. S13). These results indicate that increasing $-CF_3$ substitution strengthens the thermodynamic driving force and interfacial interactions at the donor/acceptor interface, thereby promoting exciton dissociation, while improved electron mobility and charge balance further enhance charge collection. The correlation between η_{PLQ} and P_{diss} suggests a shift in the exciton decay pathway from radiative to nonradiative transitions with increasing $-CF_3$ content, providing direct evidence for improved exciton utilization efficiency. Furthermore, the impact of stepwise $-CF_3$ substitution on recombination dynamics was analyzed *via* light-intensity-dependent measurements of V_{oc} and J_{sc} (Fig. 5c and d).[45,46] The corresponding $S/(kT/q)$ and α values for CHE-Me to CHE-9F devices are 1.19/0.902, 1.17/0.998, 1.16/0.997, and 1.13/0.997, respectively. The decrease of $S/(kT/q)$ toward unity indicates effective suppression of trap-assisted recombination, while α values approaching 1 reflect enhanced carrier collection and reduced recombination losses during transport. Collectively, these findings confirm that stepwise trifluoromethylation effectively

modulates charge transport and recombination dynamics, thereby underpinning the observed improvements in FF and PCE.

To further probe the microscopic origins of the observed efficiency enhancements, femtosecond transient absorption spectroscopy (fs-TA) was employed to investigate exciton dynamics in both neat and blend films.[47,48] In neat films (Fig. S14), all four SMAs exhibit ground-state bleaching (GSB) signals at 770–870 nm and an excited-state absorption (ESA) peak at ~910 nm, characteristic of localized excitons (LEs). In blend films (Fig. 5e and f), selective excitation of the acceptor at 760 nm induces rapid GSB and ESA signals, accompanied by a negative feature in the 600–680 nm region. The synchronous decay of the acceptor GSB (~840 nm) with the rise of the donor GSB (~630 nm) confirms ultrafast hole transfer (HT) from the acceptor to the donor. Biexponential fitting of the donor GSB (Fig. 5g and h) yields two characteristic timescales: τ_1, corresponding to interfacial exciton dissociation, and τ_2, representing exciton diffusion within domains.[49] Notably, τ_1 exhibits a slight increase from 0.343 ps for the PM6:CHE-Me blend to 0.457 ps for the PM6:CHE-9F blend, yet it remains well within the subpicosecond timescale requisite for efficient charge generation. More importantly, τ_2 decreases regularly with increasing fluorination level from PM6:CHE-Me to PM6:CHE-9F (from 12.07 ps to 5.58 ps), which demonstrates that the blend system possesses an efficient exciton harvesting mechanism. We attribute this performance enhancement to the optimized phase separation and improved D/A interfacial compatibility induced by stepwise trifluoromethylation modification, which not only shortens the exciton diffusion distance but also facilitates rapid charge separation. Transient photocurrent (TPC) and transient photovoltage (TPV) decay curves measurements further reveal shortened charge extraction times (Fig. 5i; CHE-Me: 0.502 to CHE-9F: 0.167 μs) and extended carrier lifetimes (Fig. 5j; CHE-Me: 26.06 to CHE-9F: 41.52 μs), indicative of suppressed non-radiative recombination.[50,51] These improvements are attributed to the synergistic effects of stepwise trifluoromethylation: (1) strengthened noncovalent interactions enhance D/A interfacial contact, and (2) vertical compositional gradients facilitate directional charge transport toward the electrodes. Collectively, these results demonstrate that stepwise $-CF_3$ engineering allows precise control over exciton dynamics, charge separation, and transport, linking molecular design to macroscopic device performance, and providing valuable guidance for the rational development of high-efficiency SMAs.

The morphologies of the blend films based on four SMAs were characterized by tapping-mode atomic force microscopy based infrared spectroscopy (AFM-IR). AFM height images (Fig. S15) revealed that all blend films exhibited relatively smooth surfaces, and the root-mean-square (RMS) roughness gradually decreased from 1.14 nm to 0.96 nm with increasing n, indicating enhanced intermolecular π–π stacking order.[52] In addition, AFM-IR nano-infrared spectroscopy (Fig. 6a) further confirmed that all blends formed typical bicontinuous interpenetrating network structures. Notably, the phase separation scale progressively decreased with increasing *n*: 17.4 nm for PM6:CHE-Me optimized to 11.9 nm for PM6:CHE-9F (Fig. 6d and Fig. S16).[53] This trend can be attributed to the steric hindrance effect induced by the stepwise $-CF_3$ substitution, which effectively suppressed the excessive aggregation of acceptor molecules, prevented the formation of oversized domains, and facilitated the construction of a more uniform interpenetrating network. Fig. S17 further revealed that the exciton lifetimes (τ) of neat films gradually increased from CHE-Me to CHE-9F (from 0.920 to 1.348 ns), respectively. These results indicate that nonradiative energy dissipation pathways within the molecules were significantly suppressed, leading to prolonged exciton lifetimes, which are more favorable for exciton diffusion to the D/A interface and subsequent charge separation. In the CHE-Me-based blend film, the oversized domains led to exacerbated bimolecular recombination, thereby reducing the FF. In contrast, the moderate phase separation structure in the CHE-9F-based blend film constructed efficient charge transport channels and effectively suppressed space charge accumulation. This result was highly consistent with the enhanced charge mobility and improved charge balance observed in the SCLC measurements, fully verifying the critical impact of the active layer microstructure on the photovoltaic performance of the devices.

The 2D GIWAXS patterns and line-cut profiles of the blend films (Fig. 6b, e and Table S7) reveal that the evolution of the π–π stacking distances with increasing $-CF_3$ content in the blends is opposite to that observed in the neat films: from PM6:CHE-Me to PM6:CHE-6F, the π–π stacking distances gradually decrease (3.46 to 3.34 Å), whereas in PM6:CHE-9F, the π–π distance slightly increases to 3.37 Å due to the strong steric hindrance imposed by $-C(CF_3)_3$. Meanwhile, the corresponding crystalline coherence lengths (CCL) follow a non-monotonic trend, increasing initially with $-CF_3$ substitution (CHE-Me: 27.18 Å to CHE-6F: 30.23 Å) and then slightly decreasing for CHE-9F (29.14 Å). These results indicate that in the blend films, steric hindrance and dipole effects cooperatively govern molecular packing: the dipole effect enhances intermolecular π–π interactions while excessive steric hindrance slightly restricts packing, resulting in the non-monotonic variation of π–π distances. This crystallographic evolution is highly consistent with the continuous increase in μ_e, demonstrating that the short π–π stacking distances combined with high order in the acceptor domains provides efficient pathways for electron transport, thereby effectively enhancing μ_e in the blend films.

In terms of vertical phase separation, surface energy measurements reveal that stepwise $-CF_3$ substitution progressively lowers the surface energy of the acceptor molecules. This reduction drives their migration toward the film surface in order to minimize the total system energy. Consequently, film-depth-dependent light absorption spectroscopy (FLAS) measurements (Fig. 6c and Fig. S18, S19) show that,[54] while all four blends maintain relatively balanced D/A distributions across the active layer, the degree of acceptor enrichment at the film surface increases steadily from CHE-Me to CHE-9F. In addition, enhanced non-covalent interactions induced by $-CF_3$ substitution promote tighter π–π stacking of the acceptors, further facilitating the formation of a surface-enriched acceptor layer.

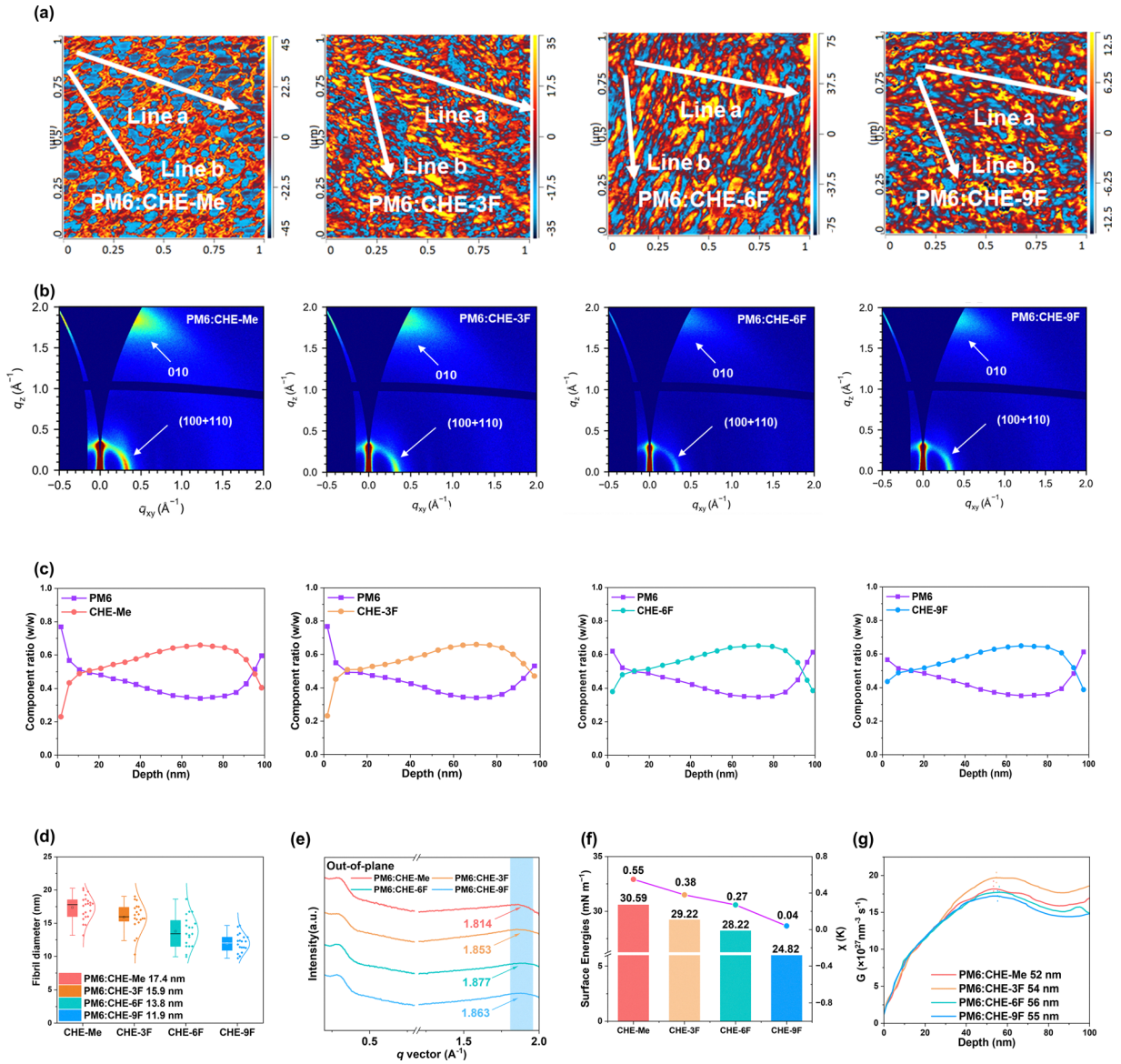

Fig. 6 (a) AFM-IR phase images of four blended films by measuring 2216 cm^{-1} signal of acceptors, in which donor and acceptor domains were marked with blue and red colors, respectively. (b) 2D GIWAXS patterns of four blended films. (c) Film-depth dependent component distribution profiles of four blended films. (d) Statistical distribution of phase separation sizes. (e) Line-cut profiles of 2D In GIWAXS patterns of four blend films in OOP. (f) Summary of the surface energy of four SMAs and their Flory–Huggins interaction parameters with PM6. (g) Dependence of simulated excitons generation rates at each wavelength as a function of film thickness.

Benefiting from the synergistic regulation of surface energy and intermolecular interactions, CHE-9F achieves an optimal vertical phase separation balance, which effectively facilitates exciton dissociation and charge transport while significantly suppressing recombination losses. Furthermore, the Flory–Huggins interaction parameters $\chi_{D/A}$ between PM6 and the four SMAs (Fig. 6g, Fig. S20 and Table S7)[55,56] decrease from 0.55 (PM6:CHE-Me) to 0.04 (PM6:CHE-9F) with increasing $-CF_3$ content, indicating significantly enhanced compatibility between the acceptor and PM6. Exciton vertical diffusion lengths in the blend films (Fig. 6h) also increase with $-CF_3$ content, measured as 52, 54, 56, and 55 nm, further confirming that optimized vertical phase separation promotes exciton transport and charge separation. Taken together, stepwise trifluoromethylation precisely regulates the blend film microstructure by synergistically optimizing π–π stacking, molecular order, and vertical phase separation. This morphological optimization not only enhances exciton diffusion and dissociation efficiency but also establishes efficient charge transport pathways, providing a foundation for the observed improvements in electron mobility, FF, and PCE.

Conclusions

In summary, a series of SMAs (CHE-*n*F, *n* = 3, 6, 9) were systematically designed *via* stepwise trifluoromethyl substitution of

CHE-Me to harness substituent-induced steric hindrance, dipole effects, and reduced surface energy for precise control over active layer morphology. Detailed investigations demonstrate that progressive substitution from $-CF_3$ to $-C(CF_3)_3$ incrementally enhances steric and dipole effects while lowering surface energy. These synergistic factors collectively optimize the photoactive layer: (1) increased steric hindrance suppresses acceptor over-aggregation, limiting domain size and enabling a uniform interpenetrating network; (2) enhanced molecular dipoles strengthen donor/acceptor interactions, shorten π–π stacking distances, confine phase separation within the exciton diffusion length, and suppress trap-assisted recombination; and (3) reduced surface energy induces vertical phase gradients, facilitating directional charge transport and improving charge collection. Leveraging these effects, the binary PM6:CHE-9F devices achieve balanced photovoltaic performance with a PCE of 19.32% and a high FF of 82.09%. When CHE-9F is incorporated as the third component into the three systems (PM6:BO-4Cl, PM6:btp-eC9, and D18:L8-BO) respectively, the corresponding ternary devices further boost the PCE to 20.01%, 20.10%, and 20.30%. Thus, this work establishes a $-CF_3$-based "steric–dipole–surface energy" synergistic regulation strategy, enabling precise morphological control and providing a rational molecular design approach toward high-performance OSCs.

Author contributions

Jie. Wang. Conducted the acceptor synthesis experiments and wrote the original paper. Xin. Chen. Fabricated and characterized the photovoltaic devices. Jingyi Huo, Collection and collation of device data. Jiong. Yang. Assisted in the synthesis of the acceptor molecule and the collection of NMR spectra. Longyu Li. Fabricated large-area modular devices. Wendi Shi. Grazing incidence wide-angle X-ray scattering (GIWAX) measurement. Ruibin Bian. Density functional theory (DFT) theoretical calculation. Wenkai Zhao. Femtosecond transient absorption spectroscopy (fs-TAS) measurement. Xianjian. Wan, and Yongsheng. Chen supervised and directed this project. All authors discussed the results and commented on the manuscript.

Conflicts of interest

The authors declare that they have no known competing financial interests or personal relationships that could have appeared to influence the work reported in this paper.

Data availability

Data will be made available on request.

Supplementary information (SI) is available. See DOI: https://doi.org/10.1039/d5ee07321a.

CCDC 2502135–2502137 contain the supplementary crystallographic data for this paper.[57a–c]

Acknowledgements

The authors gratefully acknowledge the financial support from Ministry of Science and Technology of China (2022YFB4200400) and National Natural Science Foundation (52025033, 52373189, 22361132530).

Notes and references

1 Y. Lin, J. Wang, Z. G. Zhang, H. Bai, Y. Li, D. Zhu and X. Zhan, *Adv. Mater.*, 2015, **27**, 1170–1174.
2 J. Yuan, Y. Zhang, L. Zhou, G. Zhang, H.-L. Yip, T.-K. Lau, X. Lu, C. Zhu, H. Peng, P. A. Johnson, M. Leclerc, Y. Cao, J. Ulanski, Y. Li and Y. Zou, *Joule*, 2019, **3**, 1140–1151.
3 Y. Cui, H. Yao, J. Zhang, K. Xian, T. Zhang, L. Hong, Y. Wang, Y. Xu, K. Ma, C. An, C. He, Z. Wei, F. Gao and J. Hou, *Adv. Mater.*, 2020, **32**, 1908205.
4 C. Li, J. Zhou, J. Song, J. Xu, H. Zhang, X. Zhang, J. Guo, L. Zhu, D. Wei, G. Han, J. Min, Y. Zhang, Z. Xie, Y. Yi, H. Yan, F. Gao, F. Liu and Y. Sun, *Nat. Energy*, 2021, **6**, 605–613.
5 Y.-J. Xue, Z.-Y. Lai, H.-C. Lu, J.-C. Hong, C.-L. Tsai, C.-L. Huang, K.-H. Huang, C.-F. Lu, Y.-Y. Lai, C.-S. Hsu, J.-M. Lin, J.-W. Chang, S.-Y. Chien, G.-H. Lee, U. S. Jeng and Y.-J. Cheng, *J. Am. Chem. Soc.*, 2023, **146**, 833–848.
6 L. Meng, Y. Zhang, X. Wan, C. Li, X. Zhang, Y. Wang, X. Ke, Z. Xiao, L. Ding, R. Xia, H.-L. Yip, Y. Cao and Y. Chen, *Science*, 2018, **361**, 1094–1098.
7 S. Guan, Y. Li, C. Xu, N. Yin, C. Xu, C. Wang, M. Wang, Y. Xu, Q. Chen, D. Wang, L. Zuo and H. Chen, *Adv. Mater.*, 2024, **36**, 2400342.
8 A. Wadsworth, Z. Hamid, J. Kosco, N. Gasparini and I. McCulloch, *Adv. Mater.*, 2020, **32**, 2001763.
9 L. Ye, H. Hu, M. Ghasemi, T. Wang, B. A. Collins, J.-H. Kim, K. Jiang, J. H. Carpenter, H. Li, Z. Li, T. McAfee, J. Zhao, X. Chen, J. L. Y. Lai, T. Ma, J.-L. Bredas, H. Yan and H. Ade, *Nat. Mater.*, 2018, **17**, 253–260.
10 S. Chen, L. Hong, M. Dong, W. Deng, L. Shao, Y. Bai, K. Zhang, C. Liu, H. Wu and F. Huang, *Angew. Chem., Int. Ed.*, 2022, **62**, e202213869.
11 X. Zhang, G. Li, S. Mukherjee, W. Huang, D. Zheng, L. W. Feng, Y. Chen, J. Wu, V. K. Sangwan, M. C. Hersam, D. M. DeLongchamp, J. Yu, A. Facchetti and T. J. Marks, *Adv. Energy Mater.*, 2021, **12**, 2102172.
12 N. Ahmad, J. Yuan and Y. Zou, *Energy Environ. Sci.*, 2025, **18**, 5093–5158.
13 X. Liu, C. Zhang, C. Duan, M. Li, Z. Hu, J. Wang, F. Liu, N. Li, C. J. Brabec, R. A. J. Janssen, G. C. Bazan, F. Huang and Y. Cao, *J. Am. Chem. Soc.*, 2018, **140**, 8934–8943.
14 K. Jiang, J. Zhang, C. Zhong, F. R. Lin, F. Qi, Q. Li, Z. Peng, W. Kaminsky, S.-H. Jang, J. Yu, X. Deng, H. Hu, D. Shen, F. Gao, H. Ade, M. Xiao, C. Zhang and A. K. Y. Jen, *Nat. Energy*, 2022, **7**, 1076–1086.
15 J. Zhang, S. Luo, H. Zhao, X. Xu, X. Zou, A. Shang, J. Liang, F. Bai, Y. Chen, K. S. Wong, Z. Ma, W. Ma, H. Hu, Y. Chen and H. Yan, *Angew. Chem., Int. Ed.*, 2022, **61**, e202206930.

16 W. Liang, L. Chen, Z. Wang, Z. Peng, L. Zhu, C. H. Kwok, H. Yu, W. Xiong, T. Li, Z. Zhang, Y. Wang, Y. Liao, G. Zhang, H. Hu and Y. Chen, *Adv. Energy Mater.*, 2024, **14**, 2303661.
17 X. Zhou, W. Liang, R. Ma, C. Zhang, Z. Peng, T. A. Dela Peña, J. Wu, Z. Ma, Y. Liao, G. Li and H. Hu, *Energy Environ. Sci.*, 2024, **17**, 7762–7771.
18 K. An, W. Zhong, F. Peng, W. Deng, Y. Shang, H. Quan, H. Qiu, C. Wang, F. Liu, H. Wu, N. Li, F. Huang and L. Ying, *Nat. Commun.*, 2023, **14**, 2688.
19 J. Dong, Y. Li, C. Liao, X. Xu, L. Yu, R. Li and Q. Peng, *Energy Environ. Sci.*, 2025, **18**, 4982–4995.
20 T. Zhang, H. Chen, C. Li, K. Lu, L. Zhang, A. Shokrieh, J. Zhang, G. Lu, S. Lei and Z. Wei, *J. Mater. Chem. A*, 2022, **10**, 8837–8845.
21 M. Lv, Q. Wang, J. Zhang, Y. Wang, Z. G. Zhang, T. Wang, H. Zhang, K. Lu, Z. Wei and D. Deng, *Adv. Mater.*, 2023, **36**, 2310046.
22 S. Oh, K. Bae, D. Jeong, T. N. L. Phan, J. W. Lee and B. J. Kim, *Adv. Funct. Mater.*, 2025, **35**, 2502707.
23 Y. Cho, Z. Sun, G. Li, D. Zhang, S. Yang, T. J. Marks, C. Yang and A. Facchetti, *J. Am. Chem. Soc.*, 2024, **147**, 758–769.
24 Y.-X. Lu, J.-W. Zou, Q.-S. Yu, Y.-J. Jiang and W.-N. Zhao, *Chem. Phys. Lett.*, 2007, **449**, 6–10.
25 C. Dalvit, C. Invernizzi and A. Vulpetti, *Chem. – Eur. J.*, 2014, **20**, 11058–11068.
26 H. Chen, H. Liang, Z. Guo, Y. Zhu, Z. Zhang, Z. Li, X. Cao, H. Wang, W. Feng, Y. Zou, L. Meng, X. Xu, B. Kan, C. Li, Z. Yao, X. Wan, Z. Ma and Y. Chen, *Angew. Chem., Int. Ed.*, 2022, **61**, e202209580.
27 X. Zhu, G. Zhang, J. Zhang, H.-L. Yip and B. Hu, *Joule*, 2020, **4**, 2443–2457.
28 X. Wan, C. Li, M. Zhang and Y. Chen, *Chem. Soc. Rev.*, 2020, **49**, 2828–2842.
29 H. Hu, M. Ghasemi, Z. Peng, J. Zhang, J. J. Rech, W. You, H. Yan and H. Ade, *Adv. Mater.*, 2020, **32**, 2005348.
30 P. Xue, A. M. Calascibetta, K. Chen, K. E. Thorn, Y. Jiang, J. Shi, B. Jia, M. Li, J. Xin, G. Cai, R. Yang, H. Lu, S. Mattiello, Y. Liu, Z. Tang, W. Ma, X. Lu, Q. Meng, J. M. Hodgkiss, L. Beverina, R. P. S. Han and X. Zhan, *J. Mater. Chem. A*, 2022, **10**, 24073–24083.
31 Y. Shi, Y. Chang, K. Lu, Z. Chen, J. Zhang, Y. Yan, D. Qiu, Y. Liu, M. A. Adil, W. Ma, X. Hao, L. Zhu and Z. Wei, *Nat. Commun.*, 2022, **13**, 3256.
32 M. Zhang, Z. Wang, L. Zhu, R. Zeng, X. Xue, S. Liu, J. Yan, Z. Yang, W. Zhong, G. Zhou, L. Kan, J. Xu, A. Zhang, J. Deng, Z. Zhou, J. Song, H. Jing, S. Xu, Y. Zhang and F. Liu, *Adv. Mater.*, 2024, **36**, 2407297.
33 P. Müller-Buschbaum, *Adv. Mater.*, 2014, **26**, 7692–7709.
34 X. Cao, J. Guo, Z. Li, X. Bi, H. Liang, Z. Xiao, Y. Guo, X. Jia, Z. Xu, K. Ma, Z. Yao, B. Kan, X. Wan, C. Li and Y. Chen, *ACS Energy Lett.*, 2023, **8**, 3494–3503.
35 Y. Zou, H. Chen, X. Bi, X. Xu, H. Wang, M. Lin, Z. Ma, M. Zhang, C. Li, X. Wan, G. Long, Y. Zhaoyang and Y. Chen, *Energy Environ. Sci.*, 2022, **15**, 3519–3533.
36 I. Ramirez, M. Causa, Y. Zhong, N. Banerji and M. Riede, *Adv. Energy Mater.*, 2018, **8**, 1703551.
37 M. Gruber, J. Wagner, K. Klein, U. Hörmann, A. Opitz, M. Stutzmann and W. Brütting, *Adv. Energy Mater.*, 2012, **2**, 1100–1108.
38 S. Liu, J. Yuan, W. Deng, M. Luo, Y. Xie, Q. Liang, Y. Zou, Z. He, H. Wu and Y. Cao, *Nat. Photonics*, 2020, **14**, 300–305.
39 X.-K. Chen, D. Qian, Y. Wang, T. Kirchartz, W. Tress, H. Yao, J. Yuan, M. Hülsbeck, M. Zhang, Y. Zou, Y. Sun, Y. Li, J. Hou, O. Inganäs, V. Coropceanu, J.-L. Bredas and F. Gao, *Nat. Energy*, 2021, **6**, 799–806.
40 W. Gao, F. Qi, Z. Peng, F. R. Lin, K. Jiang, C. Zhong, W. Kaminsky, Z. Guan, C. S. Lee, T. J. Marks, H. Ade and A. K. Y. Jen, *Adv. Mater.*, 2022, **34**, 2202089.
41 Q. Liu, S. Smeets, S. Mertens, Y. Xia, A. Valencia, J. D'Haen, W. Maes and K. Vandewal, *Joule*, 2021, **5**, 2365–2379.
42 Y. Qin, S. Zhang, Y. Xu, L. Ye, Y. Wu, J. Kong, B. Xu, H. Yao, H. Ade and J. Hou, *Adv. Energy Mater.*, 2019, **9**, 1901823.
43 Z. Han, C. E. Zhang, T. He, J. Gao, Y. Hou, X. Gu, J. Lv, N. Yu, J. Qiao, S. Wang, C. Li, J. Zhang, Z. Wei, Q. Peng, Z. Tang, X. Hao, G. Long, Y. Cai, X. Zhang and H. Huang, *Angew. Chem., Int. Ed.*, 2024, **63**, e202318143.
44 C. M. Proctor, S. Albrecht, M. Kuik, D. Neher and T. Q. Nguyen, *Adv. Energy Mater.*, 2014, **4**, 1400230.
45 L. Lu, T. Xu, W. Chen, E. S. Landry and L. Yu, *Nat. Photonics*, 2014, **8**, 716–722.
46 Z. Li, J. D. A. Lin, H. Phan, A. Sharenko, C. M. Proctor, P. Zalar, Z. Chen, A. Facchetti and T. Q. Nguyen, *Adv. Funct. Mater.*, 2014, **24**, 6989–6998.
47 R. Wang, C. Zhang, Q. Li, Z. Zhang, X. Wang and M. Xiao, *J. Am. Chem. Soc.*, 2020, **142**, 12751–12759.
48 L. Zhan, S. Li, Y. Li, R. Sun, J. Min, Y. Chen, J. Fang, C. Q. Ma, G. Zhou, H. Zhu, L. Zuo, H. Qiu, S. Yin and H. Chen, *Adv. Energy Mater.*, 2022, **12**, 2201076.
49 Z. Luo, W. Wei, R. Ma, G. Ran, M. H. Jee, Z. Chen, Y. Li, W. Zhang, H. Y. Woo and C. Yang, *Adv. Mater.*, 2024, **36**, 2407517.
50 V. V. Brus, C. M. Proctor, N. A. Ran and T. Q. Nguyen, *Adv. Energy Mater.*, 2016, **6**, 1502250.
51 Y. Zeng, D. Li, Z. Xiao, H. Wu, Z. Chen, T. Hao, S. Xiong, Z. Ma, H. Zhu, L. Ding and Q. Bao, *Adv. Energy Mater.*, 2021, **11**, 2101338.
52 F. Zhao, C. Wang and X. Zhan, *Adv. Energy Mater.*, 2018, **8**, 1703147.
53 Z. Chen, J. Zhu, D. Yang, W. Song, J. Shi, J. Ge, Y. Guo, X. Tong, F. Chen and Z. Ge, *Energy Environ. Sci.*, 2023, **16**, 3119–3127.
54 L. Wen, H. Mao, M. Ban, L. Tan, J. Zhang, Z. Qin, L. Zhang and Y. Chen, *Adv. Mater.*, 2025, **37**, 2503813.
55 K. Gao, S. B. Jo, X. Shi, L. Nian, M. Zhang, Y. Kan, F. Lin, B. Kan, B. Xu, Q. Rong, L. Shui, F. Liu, X. Peng, G. Zhou, Y. Cao and A. K. Y. Jen, *Adv. Mater.*, 2019, **31**, 1807842.
56 Y. Gong, T. Zou, X. Li, S. Qin, G. Sun, T. Liang, R. Zhou, J. Zhang, J. Zhang, L. Meng, Z. Wei and Y. Li, *Energy Environ. Sci.*, 2024, **17**, 6844–6855.
57 (*a*) CCDC 2502135: Experimental Crystal Structure Determination, 2026, DOI: 10.5517/ccdc.csd.cc2pzp1f; (*b*) CCDC 2502136: Experimental Crystal Structure Determination, 2026, DOI: 10.5517/ccdc.csd.cc2pzp2g; (*c*) CCDC 2502137: Experimental Crystal Structure Determination, 2026, DOI: 10.5517/ccdc.csd.cc2pzp3h.

